Supplementary Information:

Intergenerational neural mediators of early-life anxious temperament

Andrew S. Fox[a,b,c,1], Jonathan A. Oler[a,c], Alexander J. Shackman[d], Steven E. Shelton[a], Muthuswamy Raveendran[e], D. Reese McKay[f], Alexander K. Converse[b], Andrew Alexander[b,g], Richard J. Davidson[a,b,c,h], John Blangero[i], Jeffrey Rogers[e], and Ned H. Kalin[a,b,c,h,1]

[a]HealthEmotions Research Institute, University of Wisconsin–Madison, Madison, WI 53709; [b]Waisman Center, University of Wisconsin–Madison, Madison, WI 53709; [c]Department of Psychiatry, University of Wisconsin–Madison, Madison, WI 53709; [d]Department of Psychology, University of Maryland, College Park, MD 20742; [e]Department of Genetics, Baylor College of Medicine, Houston, TX 77030; [f]Department of Psychiatry, Yale School of Medicine, New Haven, CT 06519; [g]Department of Medical Physics, University of Wisconsin–Madison, Madison, WI 53709; [h]Department of Psychology, University of Wisconsin–Madison, Madison, WI 53709; and [i]Texas Biomedical Research Institute, San Antonio, TX 78245

Including:

Supplementary Results/Discussion (with Figures) (pg. 2-6)
Supplementary Methods (pg. 6-12)
Supplementary References (pg. 12-13)
Supplementary Legends (pg. 14)
Supplementary Tables (pg. 15-17)

Ned H. Kalin, M.D.
Chair Department of Psychiatry
HealthEmotions Research Institute
University of Wisconsin-Madison
6001 Research Park Blvd
Madison, WI 53719, USA
(608) 263-6079 office
(608) 263-9340 fax
nkalin@wisc.edu

Andrew S. Fox, Ph.D.
HealthEmotions Research Institute
University of Wisconsin-Madison
6001 Research Park Blvd
Madison, WI 53719, USA
(608) 301-5531 office
(608) 263-9340 fax
asfox@wisc.edu

Supplemental Results & Discussion

Brain metabolism and the components of AT

To ensure that the relationship between the composite measure of AT and brain metabolism was not primarily determined by an individual component of the composite AT phenotype, we performed three separate voxelwise regressions between NEC-related FDG-uptake and freezing, cooing, and cortisol. Results demonstrated significant relationships between brain metabolism and each AT-component, i.e. freezing, cooing and cortisol (Fig S1a, all Šidák corrected p's<.05). We then sought to determine if the three components of AT were likely to share a neural substrate by examining the spatial correlation of AT-relatedness across voxels. Although the components of AT are not highly related (see (*1*)), spatial correlations across voxels demonstrate a similar pattern of brain-phenotype relationships between components of AT (Fig S1b, $r^2_{[\text{Freezing,Cooing}]}$=.71; c, $r^2_{[\text{Freezing,Cortisol}]}$=.37; d, $r^2_{[\text{Cooing,Cortisol}]}$=.40; all p's<.0001). While the scatter plots reveal some phenotype specific voxels, most of the regions that we highlight commonly relate to each of our three anxiety-related measures. Consistent with our previous research, these data suggest that the components of AT are, in part, associated with a shared neural substrate for anxiety-related responding (*1*, *2*). For these reasons, we have focused on AT as a whole. It will be critical for future research to further differentiate general AT-related regions, from those that specifically relate to a particular phenotypic expression of anxiety.

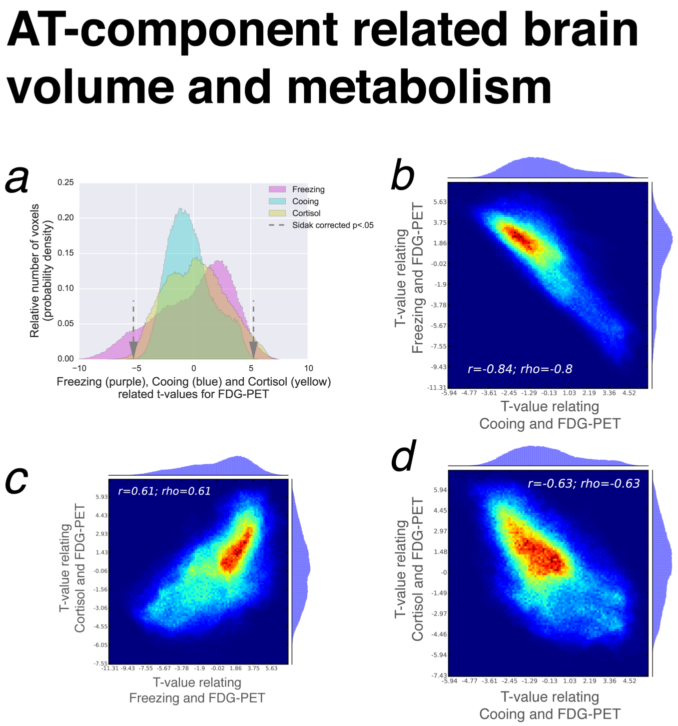

Figure S1: Histograms displaying the distribution of t-values reflecting the relationship between brain metabolism and each component of AT, i.e. freezing, cooing, and cortisol can be seen in (**a**). Grey arrows represent the threshold for reaching significance at a Šidák corrected p<.05. Although the components of AT are not highly related (see (*1*)), spatial correlations across voxels demonstrate a similar pattern of brain-phenotype relationships between components of AT (**b**, $r^2_{[\text{Freezing,Cooing}]}$=.71; c, $r^2_{[\text{Freezing,Cortisol}]}$=.37; d, $r^2_{[\text{Cooing,Cortisol}]}$=.40; all p's<.0001).

Cross-validation analysis of imaging-AT relationships

To obtain reliable estimate of the utility of brain metabolism and local brain volume in predicting extreme early-life AT, we performed supervised learning analyses with repeated cross-validation. These analyses use every brain voxel as a predictor and AT as the outcome variable. Analyses were performed separately for brain metabolism (i.e. FDG-PET) and local brain volume (i.e. log jacobian determinant). Prior to statistical analysis, each voxel was residualized for the potentially confounding effects of age, sex, site, MRI scanner, prior exposure to NEC, scan order, and affine registration parameters. These residuals were used as predictors in regression analyses.

Receiver operating characteristic curve for brain metabolism and brain volume in predicting extreme AT

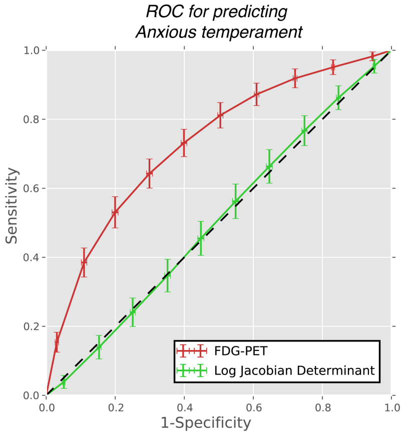

Figure S2: ROC curves using FDG-PET (red) and log jacobian determinant (green) to predict AT using elastic net regularized regressions. The dashed black line indicates chance predictions, and curves that near the upper left corner represent better predictors of AT.

Cross-validation techniques were used to compute voxelwise parameter estimates in a training dataset and use those parameter estimates to examine a test dataset. The training (four-fifths: n= 473) and test (one-fifth: n=119) samples were randomly drawn from the set of 592 subject scans. Supervised learning was performed using an elastic net regularized regression to estimate the best-fitting set of voxels and parameter estimates to predict AT in the training sample, using AT as the dependent measure and all voxels as predictors (*3*). These voxels and parameter estimates were then used to compute the estimated levels of AT in each subject in the test sample. When the number of predictors is greater than the number of samples, standard regression techniques will fail, as the set of linear equations becomes over-parameterized and rank-deficient. Regularized regression techniques provide a reasoned method for selecting which voxels best predict the AT phenotype and how to optimally weight them. Elastic net regularization combines the LASSO and ridge-regression approaches to prevent over-fitting of the data and punish overly-sparse solutions. Elastic net regularization was used to 'lightly' regularize the regression (i.e. lasso & ridge parameters λ_1=.001, λ_2=.009, respectively). The amount of variance explained was defined as the square of the correlation coefficient between the predicted and actual AT values in the test sample. To estimate the amount of variance that could be predicted, this procedure was repeated 1000 times.

To determine the utility of brain metabolism and brain volume in predicting extreme AT, we performed cross-validation analyses to determine the sensitivity and specificity of our AT-prediction. Receiver operating characteristic (ROC) curves were computed for classification of individuals into a high-AT groups defined at various percentiles (i.e. 0, 5, 15, 25, 35, 45, 55, 65, 75, 85, 95, 100). Sensitivity was computed as the number of correctly predicted AT-individuals divided by the total number of high-AT individuals in the test-set, while specificity was measured as the number of correctly predicted non high-AT individuals divided by the total number of non high-AT individuals in the test-set. Predictive measures should ideally result in high sensitivity and specificity. Complementing our univariate analyses in the full sample, cross-validation of extreme-AT prediction demonstrated significant predictive validity for FDG-PET, but not for the log jacobian determinant (Fig S2). Similar analyses were performed to examine the relationship between neuroimaging measures and the components of AT (i.e. Freezing, Cooing, and Cortisol). Like to AT, examination of the relationship between neuroimaging measures and each of AT's components revealed significant predictive validity for FDG-PET, but not for the log jacobian determinant (Fig S3).

These results indicate that there is valuable AT-related information in the FDG-PET data, but fail to support the hypothesis that early-life AT is associated with altered regional brain volume.

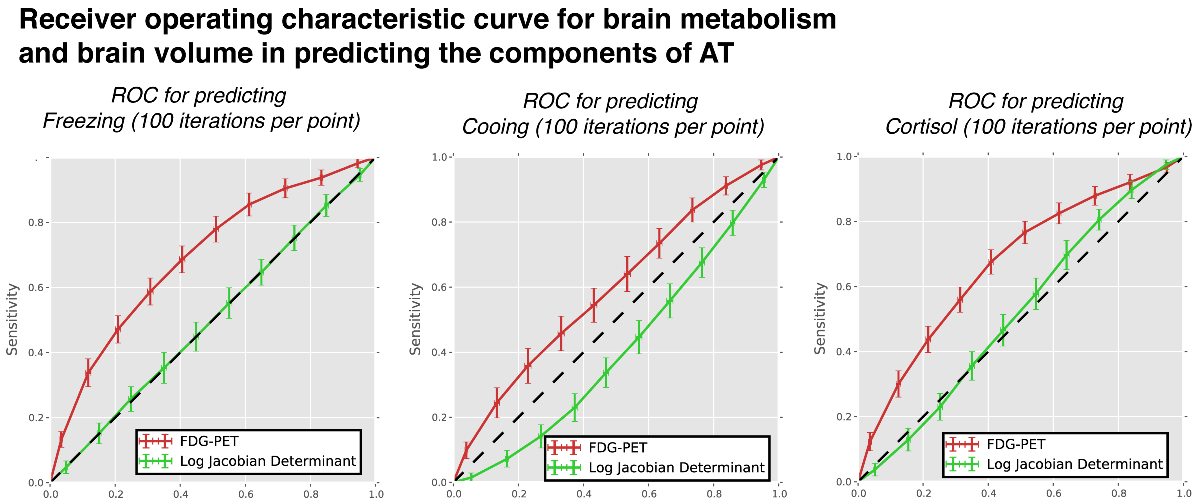

Figure S3: ROC curves using FDG-PET (red) and log jacobian determinant (green) to predict Freezing (left), Cooing (middle) and Cortisol (right) using elastic net regularized regressions. The dashed black line indicates chance predictions, and curves that near the upper left corner represent better predictors of AT.

Heritability of brain metabolism

The FDG-PET findings in this manuscript replicate and extend our previously published work, which were performed in the initial subjects from this sample (n=238/592;(*4*)). In n=238 we found heritability differed across AT's neural substrates. Of particular interest, we found that anterior hippocampal metabolism was heritable, whereas Ce metabolism was not. This finding replicates in the non-overlapping portion of the present sample (n=354/592; FDR q< .05). Power analyses revealed that we had a ~35% chance of detecting a voxel that was 25% heritable as different from zero in the initial sample, whereas in the combined n=592 sample we obtained ~95% power for this same test. In n=592, although some Ce voxels failed to reach significance, we also identified heritable voxels within the Ce-region (i.e. peak h^2 in Ce: p=.0003). Consistent with our prior work, the peak hippocampal metabolism was observed to be nearly twice as heritable (e.g. peak h^2 in aHip=.50). The differential heritability of ATs neural substrates provides important information that can help us to understand the biology of anxiety. In particular, these data suggest that different genetic pathways are likely to influence the function of the amygdala and anterior hippocampus. Moreover, by extending these results to include genetic correlation analyses, we can begin to identify those regions that are most likely to mediate the heritable risk to develop anxiety and depressive disorders (See main text as well as Figure S4).

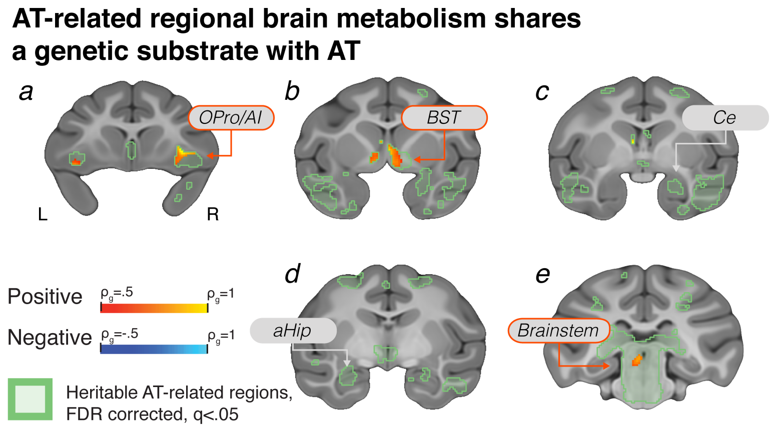

Figure S4: Regions where brain metabolism showed a significant genetic correlation with AT include include ortibal proisocortex/anterior insula (OPro/AI; shown in [a]), bed nucleus of the stria terminalis (BST; shown in [b]), and periaqueductal gray (PAG; shown in [e]), with no significant results in central nucleus of the amygdala (Ce; shown in [c]), anterior hippocampus (aHip; shown in [d]) or other brainstem regions (shown in [e]).

Identifying candidate genes using publically available databases

To begin the process of identifying molecules that might mediate the heritable component of the risk to develop anxiety and depressive disorders, we examined regional variation in the levels of gene expression from publically available human brain data. Specifically, we compared gene expression in regions genetically correlated with both AT and each other, to gene expression in the rest of the brain. By virtue of their preferentially high expression in brain regions that mediate the intergenerational transfer of AT, these genes are candidates for future mechanistic studies aimed at identifying the molecular underpinnings of the heritable risk to develop anxiety and depressive disorders. All analyses were performed based on microarray-measured gene expression in the human brain using the differential expression tool at *http://human.brain-map.com*, provided by the Allen Institute for Brain Science (AIBS)(*5*). These analyses are not intended to implicate genetic variation within these genes in AT. Rather, these analyses based on our non-human primate brain imaging data aim to provide researchers with a list of potential molecular systems within the tripartite OPro/AT-BST-PAG circuit that may contribute to the intergenerational transmission of anxiety. Because our between-region genetic correlation analyses revealed significant genetic correlations in the metabolism between BST and both PAG and OPro/AI, we targeted differential gene expression searches to those genes preferentially expressed in regions most homologous to our BST-PAG and BST-OPro/AI clusters. Specifically, independent differential gene expression searches were performed in the corresponding BST-PAG (i.e. central gray of the midbrain similar to PAG, and left bed nucleus of stria terminalis [“CGMB BST-L”] versus all gray matter [“GM”]) and BST-OPro/AI regions (i.e. posterior orbital gyrus similar to OPro, short insular gyrus similar to AI, and left bed nucleus of stria terminalis [“POrG SIG BST-L”] versus all gray matter [“GM”]) of the human brain. These tests were used to identify the top 200 genes with the greatest fold-change increase in expression between POrG, SIG, & BST-L compared to the rest of the brain (Dataset S2a), and a similar list of the top 200 genes with the greatest fold-change increase in expression in PAG & BST-L compared to the rest of the brain (Dataset S2b). We restricted these exploratory analyses to genes that showed greater expression in target areas compared to the rest of the brain, as interpreting relatively decreased expression as unrelated to the heritability of AT would require: 1) accepting that these are true null findings, and 2) assuming that lack of expression in human brains during adulthood implies that these molecules do not play a role in the cross-generational transfer of AT. Analyses revealed several well-known molecules implicated in stress-related psychopathology (e.g. serotonin transporter [SLC6A4], corticotropin-releasing hormone [CRH]), as well as several promising targets for stress-related intervention (e.g. neuropeptide Y [NPY], somatostatin [SST], and serotonin receptor 2C [HTR2C]), and several molecules that represent novel candidates for examination in relation to AT (Dataset S2). Based on our genetic correlation analyses, the genes in these lists are reasonable candidates for contributing to the function of the tripartite OPro/AI-BST-PAG circuit and the heritable components of AT.

In order to assess the relevance of these gene lists to anxiety, and to identify broader anxiety-relevant molecular processes, we performed gene ontology analyses using Enrichr (*6*). Specifically, using gene set enrichment analyses, we examined the relative number of genes identified in Dataset S2 that belong to curated gene-sets with known functions (*7*). These analyses revealed an over-representation of genes in the Biological Processes (n=75; Dataset S3a), Cellular Component (n=15; Dataset S3b), and Molecular Function ontologies (n=25; Dataset S3c). Specific over-represented ontologies include, “neuropeptide hormone activity” (GO:0005184), “synapse part” (GO:0044456), and “behavioral fear response” (GO:0001662). These informatics-based proposals for molecular processes contributing to the function of the tripartite prefrontal-limbic-midbrain circuit, provide a “proof-of-concept” for combining our large-scale brain imaging studies in non-human primates with publically-available neurogenetic datasets to gain translational insight. A deeper understanding of the mechanisms and regulators of regional gene expression will continue to refine these candidates for the molecules responsible for the heritable risk to develop anxiety and depressive disorders.

Supplementary Methods

Method overview

Each animal was injected with FDG and exposed to the NEC-context in which a human intruder presents their profile to the monkey for 30-minutes prior to receiving a PET scan. This paradigm allows us to obtain a measurement of integrated regional brain metabolism during exposure to the NEC-context. Brain metabolism was regressed against AT to identify AT-related brain regions. Heritability of local brain volume and brain metabolism was estimated at each voxel based on each pair of animals' degree of relatedness. Bivariate heritability estimates were similarly computed to examine the degree to which AT and regional brain metabolism share a genetic substrate. All experiments were performed according to the federal guidelines of animal use and care and with the approval of the University of Wisconsin Madison Institutional Animal Care and Use Committee.

Subjects

Five hundred and ninety-four young rhesus monkeys that were part of a large multi-generational pedigree were phenotyped for brain metabolism and stress-related behaviors. Paternity tests were performed when paternity was in question, which resulted in 2 animals being excluded from all analyses, resulting in five hundred and ninety-two animals included in all analyses (Age: μ=1.88, sd=0.78; 327M/265F; see histogram below). All animals were mother-reared, and pair-housed in a vivarium on a 12 hour light/dark cycle with a 6 am light onset at the Harlow Primate Laboratory and the Wisconsin National Primate Research Center. All studies were performed during the light cycle. We attempted to test every young rhesus monkey at the University of Wisconsin-Madison's Harlow Lab and Primate Center that was available for study. The availability of animals during the period data collection determined the final sample size. Animals that underwent prior drug administration or surgery were excluded. Although, a small number of animals underwent prior behavioral testing at some point in their lives as a part of experiments in other laboratories, these effects were considered to be random with respect to the effects of interest, part of the environmental influences, and were, therefore, not specifically examined. The typical life span of a rhesus macaque is approximately 25, and since most animals are weaned between 6 months and 1 year and begin puberty when they are between 3 and 4 years old, the majority of animals are considered to be roughly equivalently aged to pre-pubescent children between 3-12 years old.

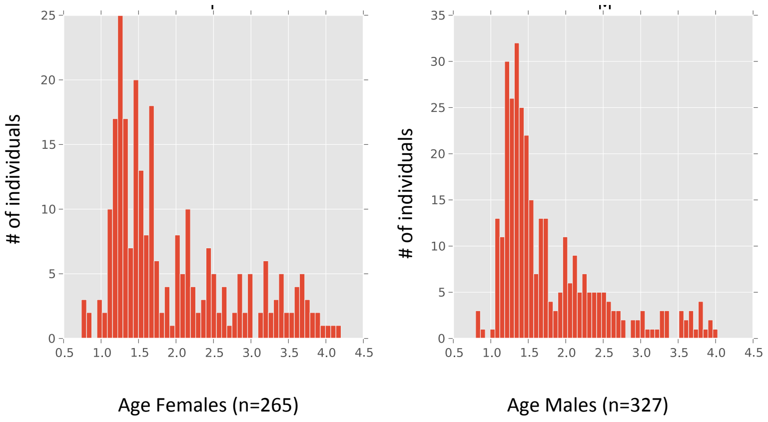

Multi-generational family pedigree

Subjects were part of a large multi-generational pedigree of 1928 animals across 8 generations. Scanned subjects from this pedigree consisted of 592 animals, with 350,464 possible relationships. The structure of this multi-generational pedigree consists of: 2 parent-offspring pairs, 28 full-sibling pairs, 44 other pairs of 1st degree relatives, 11 avuncular pairs, 1340 half sibling pairs, 1388 other pairs of 2nd degree relatives, 3293 pairs of 3rd degree relatives, 6991 pairs of 4th degree relatives, 73138 pairs of animals related less than 4th degree, and 83419 unrelated pairs.

No-Eye-Contact (NEC) context

In the NEC-context of the human intruder paradigm a potentially threatening human intruder stands ~2.5 meters away and presents their profile to the monkey while making no-eye-contact (NEC) for 30 minutes (*4*, *8*). In contrast to being alone or exposed to a human intruder staring at the monkey, the NEC context reliably elicits freezing behavior.

Measuring glucose metabolism using [18-F] deoxyglucose PET

Subjects received an intravenous injection of FDG immediately prior to the 30-minute NEC-context. Following 30-minute exposure to the NEC-context, whole blood was collected for quantifying cortisol and subjects were anesthetized with a 15mg/kg intramuscular injection of ketamine, intubated, and placed in the PET scanner. Anesthesia was maintained using 1-2% isoflurane gas. FDG and attenuation scans were acquired using a Siemens/Concorde microPET P4 scanner (*9*). Images were reconstructed using standard filtered-backprojection techniques with attenuation- and scatter-correction. This technique results in FDG-PET scans that represent the integrated brain metabolism throughout NEC-exposure. FDG-PET images were transformed to standard space as described below, and intensity-normalized so that the mean brain value was equivalent across individuals. A 2mm FWHM smoothing kernel was applied to account for variation in brain anatomy and registration.

Anxious Temperament (AT) measurements during NEC

AT estimates were computed based on behavior and physiology during NEC exposure as in other published work (*1*, *2*, *4*, *10*). Behavior was measured during NEC exposure by a trained rater blind to pedigree information. Freezing was defined as a lack of movement for greater than 3-seconds, and was scored in seconds per 5-min of NEC exposure (30-min total). Mean freezing scores were log-scaled, and standardized after removing the linear effects of age and sex. Cooing was measured as the frequency of coo-vocalizations during each 5-min period of NEC-exposure. Mean cooing frequencies were square-root transformed, and standardized after removing the linear effects of age and sex. Plasma cortisol (µg/dL) was quantified based on samples taken immediately after NEC-exposure. Cortisol was quantified in duplicate using the DPC Coat-a-count radioimmunoassay (Siemens, Los Angeles, CA). Cortisol values were standardized after removing the linear effects of age, sex, and the time-of-day in which samples were taken. A composite measure of AT was computed as the combination of standardized freezing, reductions in cooing and cortisol measures. More specifically, freezing minus cooing plus cortisol all divided by three, as can be seen in the histograms below.

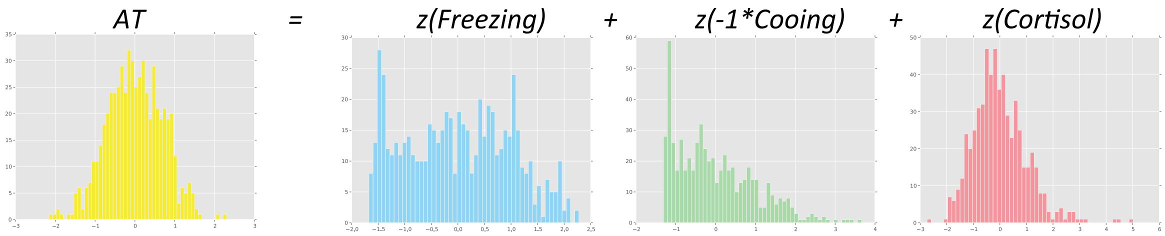

Measuring local brain volume using Magnetic Resonance Imaging (MRI)

Magnetic resonance images (MRI) were collected within 2 months of NEC-exposure. MRI was collected under anesthesia (see above) using a General Electric Discovery 3T scanner (GE Inc., Fairfield, CT) and standard quadrature extremity coil. Anatomical scans were obtained with a 3D T1-weighted, inversion-recovery, fast gradient echo prescription (TI/TR/TE/Flip/NEX/FOV/Matrix/Bandwidth: 600ms/8.65ms/1.89ms/10°/2/140mm/ 256×224/61.1 kHz) with whole brain coverage (128 slice encodes over 128 mm) reconstructed to 0.27×0.27×0.5 mm on the scanner). Each MRI scan was manually segmented into brain and non-brain tissue. T1-brain images were then transformed to standard space (methods described below), and transformation parameters were saved. The transformations to standard space were decomposed into linear (affine) and non-linear (warp) maps. The proportion of volumetric change between each animals original scan and template space was quantified as the absolute value of the jacobian determinant of the non-linear transformation. This procedure is akin to computing the number of original-space voxels that became a single voxel in template space. To put volumetric expansions and reductions on the same scale, data were log transformed. Importantly, this procedure accounts for individual differences in total brain volume. This procedure produced a single map for each subject representing the relative volume at each voxel in the brain. These log jacobian determinant maps were smoothed by 2mm in standard space, and used for statistical computations.

Study-specific template creation and individual-subject registration

We created a study-specific template because this unique dataset of 592 young rhesus monkey T1-anatomical scans together constitutes our best estimate of the macro-structure of the young rhesus monkey brain anatomy. Study-specific T1-anatomical template creation was performed using an iterative procedure using Advanced Normalization Tools (ANTS; http://sourceforge.net/projects/advants; (*11*, *12*)). Each subject's T1-anatomical image was first aligned to a predefined template-space using a non-linear symmetric diffeomorphic image registration in ANTS. Nonlinear registration was performed using a symmetric diffeomorphic image registration and a .25 gradient step-size; a pure cross correlation cost-function with window radius 2 and weight 1; the similarity matrix was smoothed with sigma=2; and this process was repeated at 4 increasingly fine levels of resolution with 30, 20, 20, and 5 iterations at each level respectively. The average of all 592 individual-subject T1's in 'template-space' was computed and taken to be the study-mean. Similarly, the non-linear deformation-field was also averaged and taken to be the deformation-mean. The deformation-mean was inverted and 15% of this deformation was applied to the study-mean, to obtain the first iteration of the study-specific template. To maintain comparability to other studies, and to printed brain atlases, the affine transformation was *not* inverted and applied to the study-mean. The same procedure was performed by aligning each subject's T1-weighted anatomical image to the initial study-specific template. After averaging the images and deformations, a new study-specific template was created by applying 15% of the newest mean-deformation to the newest study-mean. This process was repeated 4 times, to obtain a final study-specific template. Each subject's original T1-anatomical images were then aligned to this study-specific template using the ANTS non-linear registration, as previously described. Each animal's FDG-PET image was aligned to its T1-anatomical image using a rigid body mutual information warp, and the transformation from T1 to template-space was then applied to the FDG-PET image.

Measuring serotonin transporter binding using [11-C] DASB

Serotonin transporter binding was measured using the radioligand *[11-C] DASB* in a sample of 34 animals. Data from these *[C-11]DASB*-PET scans have been previously published (*13*, *14*). Methods for acquisition were fully described in (*13*). Reconstructed DASB binding estimates were transformed to the n=592 study-specific template using ANTS. Methods are identical to those described above, and transformations were applied to the DASB images.

Measuring dopamine D2/D3 receptor binding using [18-F] Fallypride

Dopamine D2/D3 receptor binding was measured using the radioligand *[18-F] Fallypride*, in a set of 33 animals. Data from these *[18-F] Fallypride*-PET scans and full methods have been previously published (*15*). Reconstructed Fallypride binging estimates were re-transformed to the n=592 study-specific template using ANTS. Methods are identical to those described above, and transformations were applied to the Fallypride images.

Statistical analysis: Voxelwise correlations

Voxelwise robust regressions between AT and brain metabolism were performed using fMRIStat (http://www.math.mcgill.ca/keith/fmristat/) and robustfit in MATLAB (http://www.mathworks.com/) (*16*). To account for potential confounds, all regressions entered potentially the confounding variables age, sex, MRI scanner, prior exposure to NEC, and order of acquisition. We implemented Šidák correction for multiple comparisons to examine AT to brain correlations (*17*).

Statistical Analysis: Spatial Correlations

To assess the similarity of the spatial relationships between voxelwise maps, we performed spatial correlations. Each image was converted to a vector, masked for voxels within the brain, and the two vectors were correlated using Pearson's and Spearman's correlations.

Statistical analysis: Heritability analyses

Heritability analyses were performed using SOLAR (http://solar.txbiomedgenetics.org/) based on pedigree information (*18*). Heritability analyses always controlled for age, age^2, sex and the age x sex interaction. Heritability analyses were performed at each voxel in the brain for both FDG-PET and log jacobian determinant with the help of the center for high-throughput computing at the University of Wisconsin-Madison and the Open Science Grid (OSG). Heritability analyses were computed as described below, and we corrected for multiple comparisons using the False Detection Rate (FDR) technique (*19*).

To estimate the heritability of a single trait (i.e. AT or brain metabolism at a single voxel), we first computed the trait's covariance matrix, which we will call Ω, where location i, j in the matrix is filled with the covariance in X between subject i and subject j.

$$\Omega_X = Cov[X, X] = \begin{bmatrix} cov(X_1, X_1) & cov(X_1, X_2) & \cdots & cov(X_1, X_n) \\ cov(X_2, X_1) & cov(X_2, X_2) & \ldots & cov(X_2, X_n) \\ \vdots & \vdots & \ddots & \vdots \\ cov(X_1, X_n) & cov(X_2, X_n) & \cdots & cov(X_n, X_n) \end{bmatrix}$$

Where covariance is defined as:

$$cov[X_i, X_j] = E[(X_i - E[X_i])(X_j - E[X_j])]$$

and, at least in this case, the expectation can be defined as:

$$E[X] = \mu(X) = \frac{1}{N} \sum_{i=1:N} X_i$$

The relatedness matrix (Φ) can be computed based on the pedigree, as:

$$\Phi = \frac{1}{2} R$$

where R is the matrix of each pair of animals relationship to each other, with the r for a parent and a child $.5 = (2^{-1})$, r for siblings $.5 = (2^{-2} + 2^{-2})$, and so on according to the table below, and beyond.

Table for relatedness matrix:

r	relationship	degree of relationship
100%	identical twins; clones	0
50%	parent-offspring	1
50%	full siblings	2
37.5%	3/4 siblings or sibling cousins	2
25%	grandparent-grandchild	2
25%	half siblings	2
25%	aunt/uncle-nephew/niece	3
25%	double first cousins	4
12.5%	great grandparent-great grandchild	3
12.5%	first cousins	4
12.5%	quadruple second cousins	6
9.38%	triple second cousins	6
6.25%	half-first cousins	4
6.25%	first cousins once removed	5
6.25%	double second cousins	6
3.13%	second cousins	6
0.78%	third cousins	8
0.20%	fourth cousins	10

Using the covariance and relatedness matrices, one can estimate the putatively genetic and environmental variance of a quantitative phenotypic trait in the form:

$$\Omega \approxeq 2\Phi\sigma_g^2 + I_n\sigma_e^2$$

where:

Ω is the covariance matrix of the phenotype
Φ is the n x n kinship matrix for the pedigree
σ_g^2 is the variance in the trait due to additive genetic (g) effects
I_n is the n x n identity matrix
σ_e^2 is the variance due to unmeasured random effects, i.e. environmental (e)

It is worth noting that the variance attributed to the environment in this mode, is considered to be random for each subject, and not shared between subjects.

The variance parameters σ can be estimated by maximizing the likelihood function:

$$\mathcal{L}(\sigma_g^2, \sigma_e^2 | y) = -\frac{n}{2}\ln(2\eta) - \frac{1}{2}\ln(\Omega) - \frac{1}{2}(x - \mu_X)'\Omega^{-1}(X - \mu_X)$$

After estimating this model, the heritability (h^2) can be estimated based on the variance in genetic and environmental effects, by calculating:

$$h^2 = \frac{\sigma_g^2}{(\sigma_g^2 + \sigma_e^2)}$$

Computing the probability of this heritability and is computed by comparing the log likelihood of the model above and the difference between this model and another where σ_g^2 is constrained to equal 0, i.e.:

$$\chi_1^2[\sigma_g^2] = -2\mathcal{L}_{\sigma_g^2=0} + 2\mathcal{L}$$

Statistical analysis: Bivariate heritability analyses

Bivariate heritability analyses were performed using SOLAR (http://solar.txbiomedgenetics.org/) based on pedigree information (*18*, *20*, *21*). Bivariate heritability analyses always controlled for age, age^2, sex and the age by sex interaction. Bivariate heritability analyses examining the shared heritability of AT and FDG-PET were performed at each voxel in the brain as described below, and were corrected for multiple comparisons using the False Detection Rate (FDR) (*19*). Because there were no significant correlations between AT and the log-jacobian determinant, bivariate heritability was not performed on this dataset. Analyses were performed at the center for high-throughput computing at the University of Wisconsin-Madison and the Open Science Grid (OSG).

Bivariate heritability analyses are performed using methods similar to the heritability analyses detailed above, with a covariance matrix that represents both traits and their interaction. More specifically,

$$\Omega_B = \begin{bmatrix} \Omega_X & \Omega_{YX} \\ \Omega_{XY} & \Omega_Y \end{bmatrix}$$

Where Ω_X and Ω_Y are as Ω above, and the bivariate portions are:

$$\Omega_{XY} \approxeq 2\Phi\sigma_{g_{XY}}^2 + I_n\sigma_{e_{XY}}^2$$

with ϕ defined as before, and the variance of X, Y can be decomposed to its component parts:

$$\sigma_{XY}^2 = \sigma_X\sigma_Y\rho_{XY}$$

where ρ_{gXY} is the genetic correlation, that we have set out to estimate.

This can now be estimated using the same maximum likelihood estimation we described above:

$$\mathcal{L}(\sigma_{g_X}^2, \sigma_{e_X}^2, \sigma_{g_Y}^2, \sigma_{e_Y}^2, \rho_{e_{XY}} | X, Y) = \quad -n\ln(2\eta) - \frac{1}{2}\ln\ |\ \Omega_B\ | \\ -\frac{1}{2}\left(\begin{bmatrix} X \\ Y \end{bmatrix} - \mu_{\begin{bmatrix} X \\ Y \end{bmatrix}}\right)'\Omega^{-1}\left(\begin{bmatrix} X \\ Y \end{bmatrix} - \mu_{\begin{bmatrix} X \\ Y \end{bmatrix}}\right)$$

As before, the three parts of this function are: a distribution parameter (now for bivariate normal), the genetic and environmental components (now including a mean), and the mean.

Similar to the test above, the p-values for s can be computed by estimating the same model with $\rho = 0$.

$$\chi_1^2[\rho_g] = -2\mathcal{L}_{\rho_g=0} + 2\mathcal{L}$$

Computing: Center for High-Throughput Computing (CHTC) and the Open Science Grid

This research was performed using resources and the computing assistance of the UW-Madison Center For High Throughput Computing (CHTC) in the Department of Computer Sciences. The CHTC is supported by UW-Madison and the Wisconsin Alumni Research Foundation, and is an active member of the Open Science Grid, which is supported by the National Science Foundation and the U.S. Department of Energy's Office of Science. All jobs were submitted using HTCondor.

Data availability

Voxelwise maps representing the AT-relatedness and heritability of brain volume and brain metabolism, can be found in supplementary Dataset 1.

Supplementary References

1. A. J. Shackman *et al.*, Neural mechanisms underlying heterogeneity in the presentation of anxious temperament, *Proc. Natl. Acad. Sci. U.S.A.* **110**, 6145–6150 (2013).

2. A. S. Fox, S. E. Shelton, T. R. Oakes, R. J. Davidson, N. H. Kalin, Trait-Like Brain Activity during Adolescence Predicts Anxious Temperament in Primates, *PLoS ONE* **3** (2008), doi:10.1371/journal.pone.0002570.

3. H. Zou, T. Hastie, Regularization and Variable Selection via the Elastic Net, *Journal of the Royal Statistical Society. Series B (Statistical Methodology)* **67**, 301–320 (2005).

4. J. A. Oler *et al.*, Amygdalar and hippocampal substrates of anxious temperament differ in their heritability, *Nature* **466**, 864–868 (2010).

5. M. J. Hawrylycz *et al.*, An anatomically comprehensive atlas of the adult human brain transcriptome, *Nature* **489**, 391–399 (2012).

6. E. Y. Chen *et al.*, Enrichr: interactive and collaborative HTML5 gene list enrichment analysis tool, *BMC Bioinformatics* **14**, 128 (2013).

7. M. Ashburner *et al.*, Gene ontology: tool for the unification of biology. The Gene Ontology Consortium, *Nat. Genet.* **25**, 25–29 (2000).

8. N. H. Kalin, S. E. Shelton, M. Rickman, R. J. Davidson, Individual differences in freezing and cortisol in infant and mother rhesus monkeys, *Behav. Neurosci.* **112**, 251–254 (1998).

9. C. Tai *et al.*, Performance evaluation of the microPET P4: a PET system dedicated to animal imaging, *Phys Med Biol* **46**, 1845–1862 (2001).

10. A. S. Fox *et al.*, Central amygdala nucleus (Ce) gene expression linked to increased trait-like Ce metabolism and anxious temperament in young primates, *Proc. Natl. Acad. Sci. U.S.A.* **109**, 18108–18113 (2012).

11. B. B. Avants *et al.*, The optimal template effect in hippocampus studies of diseased populations, *Neuroimage* **49**, 2457–2466 (2010).

12. B. B. Avants *et al.*, A reproducible evaluation of ANTs similarity metric performance in brain image registration, *Neuroimage* **54**, 2033–2044 (2011).

13. B. T. Christian *et al.*, Serotonin transporter binding and genotype in the nonhuman primate brain using [C-11]DASB PET, *Neuroimage* **47**, 1230–1236 (2009).

14. J. A. Oler *et al.*, Serotonin transporter availability in the amygdala and bed nucleus of the stria terminalis predicts anxious temperament and brain glucose metabolic activity, *J. Neurosci.* **29**, 9961–9966 (2009).

15. B. T. Christian *et al.*, The distribution of D2/D3 receptor binding in the adolescent rhesus monkey using small animal PET imaging, *Neuroimage* **44**, 1334–1344 (2009).

16. T. D. Wager, M. C. Keller, S. C. Lacey, J. Jonides, Increased sensitivity in neuroimaging analyses using robust regression, *Neuroimage* **26**, 99–113 (2005).

17. Z. Šidák, Rectangular Confidence Regions for the Means of Multivariate Normal Distributions, *Journal of the American Statistical Association* **62**, 626–633 (1967).

18. L. Almasy, J. Blangero, Multipoint quantitative-trait linkage analysis in general pedigrees, *Am. J. Hum. Genet.* **62**, 1198–1211 (1998).

19. C. R. Genovese, N. A. Lazar, T. Nichols, Thresholding of statistical maps in functional neuroimaging using the false discovery rate, *Neuroimage* **15**, 870–878 (2002).

20. L. Almasy, T. D. Dyer, J. Blangero, Bivariate quantitative trait linkage analysis: pleiotropy versus co-incident linkages, *Genet. Epidemiol.* **14**, 953–958 (1997).

21. J. T. Williams, P. Van Eerdewegh, L. Almasy, J. Blangero, Joint multipoint linkage analysis of multivariate qualitative and quantitative traits. I. Likelihood formulation and simulation results, *Am. J. Hum. Genet.* **65**, 1134–1147 (1999).

Supplementary Legends

Legend Figure S1: Histograms displaying the distribution of t-values reflecting the relationship between brain metabolism and each component of AT, i.e. freezing, cooing, and cortisol can be seen in (**a**). Grey arrows represent the threshold for reaching significance at a Šidák corrected p<.05. Although the components of AT are not highly related (see (*1*)), spatial correlations across voxels demonstrate a similar pattern of brain-phenotype relationships between components of AT (**b**, $r^2_{[\text{Freezing,Cooing}]}$=.71; c, $r^2_{[\text{Freezing,Cortisol}]}$=.37; d, $r^2_{[\text{Cooing,Cortisol}]}$=.40; all p's<.0001).

Legend Figure S2: ROC curves using FDG-PET (red) and log jacobian determinant (green) to predict AT using elastic net regularized regressions. The dashed black line indicates chance predictions, and curves that near the upper left corner represent better predictors of AT.

Legend Figure S3: ROC curves using FDG-PET (red) and log jacobian determinant (green) to predict Freezing (left), Cooing (middle) and Cortisol (right) using elastic net regularized regressions. The dashed black line indicates chance predictions, and curves that near the upper left corner represent better predictors of AT.

Legend Figure S4: Regions where brain metabolism showed a significant genetic correlation with AT include include ortibal proisocortex/anterior insula (OPro/AI; shown in [a]), bed nucleus of the stria terminalis (BST; shown in [b]), and periaqueductal gray (PAG; shown in [e]), with no significant results in central nucleus of the amygdala (Ce; shown in [c]), anterior hippocampus (aHip; shown in [d]) or other brainstem regions (shown in [e]).

Legend Table S1: Clusters that are significantly related to AT (p<.05, Sidak corrected), as well as each local maxima in each cluster that fell in a cytoarchitectonically distinct region and was at least 2mm from the nearest peak.

Legend Table S2: Clusters that are: 1) significantly related to AT (p<.05, Sidak corrected), 2) significantly heritable (FDR q<.05 within AT-related regions), and 3) significantly co-heritable with AT (FDR q<.05 within AT-related heritable regions), as well as each local-maxima within each cluster that fell in a cytoarchitectonically distinct region and was at least 2mm from the nearest peak according to the Paxinos atlas. Importantly, because of the complexity of this analysis readers should not interpret point-estimates of rho-g or non-significant findings.

Supplementary Table S1: AT-related regions

Cluster				Peak							Heritability of peak	
Region	*Direction of correlation*	*Cluster Hemisphere*	*Cluster volume (mm^2)*	*Region*	*Peak Hemisphere*	*Maximum t-value*	*p-value*	*x*	*y*	*z*	*h2*	*p*
Anterior temporal lobe & Orbitofrontal Cortex	+	Right	1090	TPO	Right	8.0727	2.00E-15	21.25	2.5	-9.375	0	1
				Ce	Right	7.6635	3.84E-14	12.5	2.5	-9.375	0.261337	0.000360489
				TEa	Right	7.1609	1.22E-12	19.375	0	-12.5	0.174347	0.000328481
				aHip	Right	7.0817	2.08E-12	15	-6.875	-10.625	0.257345	0.000152826
				Opro	Right	6.4932	9.06E-11	16.25	9.375	-1.25	0.268771	0.000128925
				TPPro	Right	6.3251	2.54E-10	21.25	6.875	-6.875	0.201427	0.00237447
				Pir	Right	5.9655	2.13E-09	13.125	3.75	-4.375	0.188983	0.0121205
				TLR(Area 36R	Right	5.6065	1.60E-08	13.75	3.75	-17.5	0.166364	0.00698572
				TE1	Right	5.5715	1.94E-08	19.375	-2.5	-13.125	0.19479	0.000189722
				ER	Right	5.4874	3.05E-08	11.875	1.875	-15	0.151739	0.00802457
Brainstem, Thalamus, Hypothalamus	+	Bilateral	2167	PAG	Right	8.9211	3.03E-18	0.625	-15	-3.75	0.188205	0.0171766
				PTg (region)	Left	8.2515	5.31E-16	-2.5	-13.75	-8.75	0.359567	3.81E-06
				3N (region)	Right	7.5539	8.30E-14	0.625	-10.625	-6.875	0.513636	0
				pHip	Left	7.2293	7.72E-13	-10	-16.875	1.25	0.188604	0.00589794
				lPul	Left	6.8106	1.22E-11	-11.25	-14.375	-1.875	0.346932	1.25E-06
				MVe (region)	Left	6.6964	2.53E-11	-1.875	-21.25	-15	0.369479	2.93E-05
				SC	Right	6.6095	4.39E-11	5.625	-13.75	-13.75	0.263692	0.00019896
				PH	Left	6.5273	7.33E-11	-1.25	-5.625	-4.375	0.324197	6.38E-06
				PH	Right	6.385	1.76E-10	2.5	-5.625	-4.375	0.344087	2.09E-06
				RLi (region)	Left	6.184	5.91E-10	-1.25	-8.75	-3.125	0.460485	1.79E-07
				lPul	Right	5.979	1.97E-09	8.75	-13.75	0.625	0.490416	0
				PR (region)	Left	5.9405	2.45E-09	-3.75	-8.125	-1.875	0.382055	5.36E-06
				APul (region)	Left	5.7907	5.76E-09	-7.5	-13.125	6.875	0.36935	1.79E-07
				MD	Right	5.6464	1.29E-08	1.25	-5.625	5	0.499351	5.96E-08
Anterior Temporal	+	Left	434	TPO	Left	7.1858	1.04E-12	-20	2.5	-12.5	0.153073	0.00567132
				TEa	Left	6.4102	1.51E-10	-16.25	2.5	-14.375	0.242928	9.40E-05
				TEM	Left	6.2393	4.25E-10	-22.5	-0.625	-12.5	0.188555	0.00140309
				Pir	Left	5.8871	3.33E-09	-11.25	5	-10	0.155765	0.0173544
				TPPro	Left	5.7371	7.77E-09	-19.375	7.5	-7.5	0.169864	0.014115
				AA	Left	5.6471	1.28E-08	-11.875	3.125	-6.25	0	1
				ST1	Left	5.4891	3.03E-08	-21.875	5.625	-6.875	0.250196	0.0013544
Hippocampus	+	Left	172	aHip	Left	7.0474	2.61E-12	-11.25	-3.125	-9.375	0.294571	4.89E-05
Extended Amygdala, Subgenual Cingulate	+	Right	155	BST	Right	6.742	1.90E-11	5.625	3.125	-1.875	0.269537	1.63E-05
				Area 25	Right	6.3999	1.61E-10	1.25	8.75	1.875	0.40679	1.19E-07
Temporal Cortex	+	Right	41	TEM	Right	6.0422	1.36E-09	28.125	-8.125	-4.375	0.229413	0.00238067
Parietal Cortex	+	Right	31	PGa	Right	6.9724	4.27E-12	20	-9.375	-1.875	0	1
Temporal Cortex	+	Left	35	TEM	Left	6.459	1.12E-10	-26.25	-10.625	-3.125	0.184614	0.00328374
Orbitofrontal Cortex	+	Left	26	Area 47	Left	5.8177	4.94E-09	-16.25	14.375	4.375	0.12429	0.0409642
				Area 13	Left	5.7168	8.70E-09	-10.625	14.375	5.625	0.164557	0.00539714
Septum	+	Right	30	LS	Right	6.0748	1.13E-09	1.875	0	6.25	0	1

Hippocampus	+	Right	16	Hip	Right	5.7616	6.78E-09	16.875	-10.625	-8.75	0.334407	5.90E-06
Visual Cortex, Parietal Cortex	-	Bilateral	7255	V1	Left	-9.1295	5.72E-19	-7.5	-20.625	13.75	0.187854	0.00480813
				PGM	Right	-8.9205	3.05E-18	9.375	-21.25	16.875	0.17998	0.00264174
				V4	Left	-8.7649	1.04E-17	-8.125	-18.75	13.125	0.158826	0.0188324
				PGM	Left	-8.7309	1.36E-17	-11.875	-26.875	0.625	0.335256	3.40E-06
				V1	Right	-8.5666	4.85E-17	6.25	-30.625	0	0.344527	6.56E-07
				V2	Left	-8.4085	1.63E-16	-5	-26.25	17.5	0.251739	9.38E-05
				LIP	Right	-8.2127	7.10E-16	10.625	-29.375	1.25	0.33002	4.05E-06
				V2	Right	-8.1754	9.37E-16	5	-34.375	-0.625	0.337413	4.17E-07
				PEa	Left	-8.0415	2.52E-15	-5	-36.25	1.25	0.30136	1.51E-05
				PEC	Right	-7.9715	4.21E-15	6.875	-33.75	8.75	0.348955	4.05E-06
				PEa	Right	-7.5088	1.14E-13	10.625	-35	1.875	0.329565	1.13E-06
				V3	Right	-7.3254	4.02E-13	2.5	-32.5	15.625	0.24428	2.72E-05
Superior Temporal Cortex	-	Right	78	MSTD	Right	-7.0493	2.57E-12	15	-21.875	6.875	0	1
Temporal Cortex	-	Left	83	TPOC	Left	-7.2556	6.47E-13	-12.5	-22.5	9.375	0.138651	0.0373646
Superior Temporal Cortex	-	Left	83	MSTD	Left	-6.1216	8.55E-10	-16.25	-24.375	10.625	0.231535	0.00296545
Motor Cortex	-	Left	497	Area 4	Left	-7.9745	4.11E-15	-12.5	-3.75	20	0.211055	6.09E-05
				Area 3	Left	-7.4147	2.18E-13	-6.875	-9.375	23.75	0.33474	0
Motor Cortex	-	Right	445	PE	Right	-7.8161	1.30E-14	11.25	-10.625	18.75	0.194055	0.00117958
				Area 3	Right	-7.2242	8.00E-13	7.5	-6.875	23.125	0.314775	0
				Area 4	Right	-7.1861	1.03E-12	10.625	-1.25	19.375	0.238066	1.31E-06

Supplementary Table S1: Clusters that are significantly related to AT (p<.05, Sidak corrected), as well as each local maxima in each cluster that fell in a cytoarchitectonically distinct region and was at least 2mm from the nearest peak.

Supplementary Table S2
Regions showing a significant genetic correlation with AT.

Cluster				Peak						
Region	*Direction of correlation*	*Cluster Hemisphere*	*Cluster volume (mm^2)*	*Region*	*Peak Hemisphere*	*Maximum rho-g*	*p-value*	*x*	*y*	*z*
Brainstem	+	Left	5.3711	Left	Edinger Westphal/ Oculomotor Nucleus (3N)	0.64	0.0080	0	-10	-3.125
BST / Nucleus Accumbens	+	Left	7.5684	Left	BST	0.75	0.0005	-2.5	3.125	-1.25
BST / Sublenticular extended amygdala / Nucleus Accumbens	+	Right	47.1191	Right	BST/Nacc	1.00	0.0006	1.25	4.375	0
Orbital/Insular Cortex	+	Right	32.7148	Right	13L	0.82	0.0005	16.875	11.25	1.875
	+			Right	OPro	1.00	0.0011	16.875	9.375	1.25
	+	Left	6.5918	Left	Opro	0.74	0.0023	-16.875	9.375	-2.5
	+			Right	47O	0.93	0.0024	20	11.25	-0.625
	+			Right	AI	0.80	0.0025	15.625	10	2.5
PAG	+	Left	15.1367	Left	PAG	0.86	0.0042	-0.625	-15.625	-3.75
White-matter	+	Right	8.7891	Right	White-matter near Area 47L and Area 45A	0.97	0.0024	18.75	15	6.25
Parietal Cortex	-	Left	5.3711	Left	MSTD	-0.94	0.0018	-11.875	-23.75	11.875
Visual and Parietal Cortex	-	Bilateral	1746.0938	Left	PEa (MIP)	-1.00	0.0000	-8.125	-23.75	16.875
Visual and Parietal Cortex	-			Right	PEa (MIP)	-1.00	0.0001	5.625	-21.875	13.125
	-			Right	V6	-0.73	0.0002	6.875	-30.625	3.75
	-			Right	V2	-0.72	0.0002	11.875	-31.25	0
	-			Right	PO (V6)	-1.00	0.0006	3.125	-33.75	7.5
	-			Left	PEa	-0.88	0.0009	-7.5	-16.25	13.125
	-			Left	V1	-0.69	0.0029	-11.25	-36.25	-1.25
	-			Right	V2	-0.63	0.0042	5	-36.25	5.625
Visual Cortex	-	Left	8.7891	Left	V2	-0.92	0.0006	-8.125	-20.625	-4.375
Visual cortex	-	Right	31.7383	Right	V1	-0.82	0.0038	5.625	-43.125	-5.625
Visual Cortex	-	Left	2.4414	Left	V3	-0.71	0.0071	-11.25	-22.5	-4.375

Supplementary Table S2: Clusters that are: 1) significantly related to AT (p<.05, Sidak corrected), 2) significantly heritable (FDR q<.05 within AT-related regions), and 3) significantly co-heritable with AT (FDR q<.05 within AT-related heritable regions), as well as each local-maxima within each cluster that fell in a cytoarchitectonically distinct region and was at least 2mm from the nearest peak according to the Paxinos atlas. Importantly, because of the complexity of this analysis readers should not interpret point-estimates of rho-g or non-significant findings.